RSC Advances

PAPER

View Article Online
View Journal | View Issue

Cite this: *RSC Adv.*, 2026, **16**, 12927

Role of acidity in acid-clay catalysts for the phosgene-free synthesis of methylene diphenyl dicarbamate (MDC)

Pengfei Chen, Junfeng Qian, Qun Chen,* Xuan Dai * and Mingyang He

The phosgene-free synthesis of methylene diphenyl diisocyanate (MDI) from dimethyl carbonate (DMC) involves the acid-catalyzed condensation of methyl *N*-phenylcarbamate (MPC) with formaldehyde (HCHO) to produce methylene diphenyl carbamate (MDC). This study investigates the catalytic properties of a commercial acidic clay (HM-X), with a focus on its acidity and Brønsted/Lewis (B/L) balance. Characterization by XRD, N_2 adsorption, NH_3-TPD, and pyridine-IR shows that HM-X has a high density of medium and strong acid sites, with a notable Brønsted component. Under certain reaction conditions in DMC with co-fed water, HM-X achieved an 88.1% MDC yield at 90 °C after 6 hours. However, excessive acidity promoted side reactions, decreasing MDC selectivity. These findings highlight the importance of optimizing Brønsted and Lewis sites to balance activity and selectivity, providing insights for designing efficient, recyclable solid acids for sustainable, phosgene-free MDI production.

Received 2nd December 2025
Accepted 1st March 2026

DOI: 10.1039/d5ra09318j

rsc.li/rsc-advances

1. Introduction

A phosgene-free route to MDI has become a priority as polyurethane production expands under increasingly stringent safety and sustainability constraints.[1–4] In these alternative schemes, DMC chemistry is particularly attractive for its atom economy, inherent safety, and integration with carbon-efficient DMC production from CO_2-derived methanol.[5–9]

In the non-phosgene MDI sequence, the acid-catalyzed condensation of MPC with formaldehyde to form MDC is rate- and selectivity-determining.[10–13] Conversion and yield depend on both the density and strength of accessible acid sites and on the B/L distribution.[11,12] Brønsted sites protonate formaldehyde to form oxonium-type intermediates, while Lewis sites polarize the carbonyl group and stabilize cationic species.[14] Excessive acidity or a high density of active sites promotes secondary condensation, oligomerization, and acetalization, lowering MDC selectivity.[15,16]

Catalyst families investigated for this transformation include homogeneous mineral acids, heteropoly acids, zeolites, sulfated oxides, and acid clays.[10–13,17–19] Homogeneous systems exhibit high intrinsic activity but suffer from corrosion and waste-handling issues.[10,17] Supported polyoxometalates (HPAs) provide tunable strong acidity in recyclable form, though leaching and hydrothermal instability remain challenges under liquid-phase conditions.[20,21]

Acid clays such as montmorillonites K10 are attractive low-cost solids featuring tunable surface acidity, slit-like mesoporosity, and predominantly Lewis-type sites with minor Brønsted contributions.[22,23] Their acidity can be modified by acid treatment, intercalation, or deposition of additional acidic functions.[23–28]

Deposition of Keggin-type Tungstophosphoric Acid (TPA) onto high-surface-area supports is a common strategy to raise site density and introduce stronger Brønsted acidity while maintaining catalyst recoverability. Dispersion state (amorphous *versus* crystallites), support interaction and porosity control are known to determine both activity and HPA stability.[29–32]

For the MPC + HCHO → MDC reaction, few studies have quantitatively correlated acidity descriptors with the activity–selectivity trade-off in DMC medium containing co-fed water. Characterizing acidity under reaction-relevant conditions is thus critical. Pyridine-adsorbed IR (Py-IR) distinguishes Brønsted ($\approx$1540 cm^{-1}) and Lewis ($\approx$1450 cm^{-1}) sites, while NH_3-TPD provides complementary distributions of weak, medium and strong sites.[33–35]

This study addresses these gaps by investigating a commercial acidic clay (HM-X) that represents a high-acidity, high-site-density case. Structural and acid-site characterization, including XRD, N_2 adsorption–desorption, NH_3-TPD, and Py-IR, are correlated with catalytic performance in the MPC and formaldehyde condensation to MDC using DMC as a solvent. Catalyst stability is further assessed relative to HM-X. The findings provide a quantitative framework linking acidity, structure, and catalytic behavior in phosgene-free MDC synthesis relevant to sustainable MDI production.

Jiangsu Key Laboratory of Advanced Catalytic Materials and Technology, Changzhou University, Changzhou 213164, China. E-mail: chmdaix@cczu.edu.cn

2. Experimental section

2.1. Materials

DMC and nitrobenzene were purchased from Sinopharm Chemical Reagent Co., Ltd MPC was obtained from Macklin Biochemical Co., Ltd TPA and montmorillonite K10 were purchased from Aladdin Biochemical Technology Co., Ltd A 37%(w/w) aqueous formaldehyde solution was supplied by Lingfeng Chemical Reagent Co., Ltd Acidic clay HM-X was purchased from Tanming Technology Co., Ltd (Hangzhou, China). All reagents were commercial and used as received.

2.2. Characterization

Powder X-ray diffraction (XRD) patterns were collected on a Rigaku SmartLab diffractometer (Japan) equipped with a Cu Kα radiation source ($\lambda = 1.5406$ Å) and a high-speed 1D detector. Crystal structure and phase composition were analyzed using Bragg's law ($2d \sin\theta = n\lambda$). FTIR spectra of the prepared catalyst were collected on a Nicolet PROTÉGÉ 460 FTIR spectrometer using KBr disks. Specific surface area, pore volume, and pore size distribution were determined from N_2 adsorption–desorption isotherms at 77 K using a Micromeritics ASAP 2460 (software v3.01). Temperature-programmed desorption of ammonia (NH_3-TPD) was performed on a Micromeritics AutoChem II 2920 chemisorption analyzer (USA) fitted with a thermal conductivity detector (TCD) and a quartz microreactor. Product compositions of reaction mixtures were analyzed by high-performance liquid chromatography (HPLC) on an Agilent 1260 Infinity II system, using nitrobenzene as the internal standard. The surface acidity was determined by pyridine adsorption FT-IR spectroscopy using a Bruker TENSOR 27 spectrometer. Following *in situ* dehydration at 300 °C in Ar, spectra were collected at 90 °C and 150 °C to probe chemisorbed pyridine.

2.3. Catalyst preparation

HM-X is a commercial acidic clay (Tanming Technology Co., Ltd, Hangzhou, China) produced *via* a proprietary acid treatment. It was used as received without further purification or modification.

2.4. Condensation of MPC with formaldehyde

The condensation of MPC with formaldehyde was carried out in DMC over solid-acid catalysts to produce MDC (Scheme 1). In a typical run, MPC, catalyst, and DMC were charged into a four-necked round-bottom flask and stirred at 70 °C. A 37% (w/w) aqueous formaldehyde solution was then added dropwise. Upon completion of the addition, the reaction temperature was raised to the desired value and maintained for the specified time. After the reaction, the mixture was cooled to room temperature and spiked with nitrobenzene as an internal standard. Quantitative analysis was performed by HPLC.

2.5. Recycling protocol

After each batch, the reaction mixture was hot-filtered to recover the solid catalyst. The recovered catalyst was washed with DMC (3×10 mL), then dried at 100 °C for 8 h and reused without further treatment. Recycling tests were conducted with the following catalyst charges: HM-X, 1.5 g. Unless stated otherwise, all other conditions were identical for each cycle: MPC 10 mmol; n(MPC)/n(HCHO) = 7; DMC 20 mL; 90 °C; 4.0 h.

3. Results and discussion

3.1. Catalyst screening

A series of solid acid catalysts was evaluated for the condensation of MPC with formaldehyde to MDC in DMC (Table 1). In the absence of a catalyst, no reaction occurred. Among the tested materials, the commercial acid clay HM-X showed the highest activity, giving an MDC yield of 76.4% at 95.2% MPC conversion. K10 and the acidic clay from Anji also displayed reasonable performance, affording MDC yields of 41.3% and 54.5%, respectively, with moderate MPC conversions.

In contrast, HM-Y and Sn-beta led to low MPC conversions and no detectable MDC under the same conditions. Zeolitic catalysts (H-ZSM-5, ZSM-5, MCM-22, HY/9-12) provided only modest MPC conversions and low MDC yields (≤ 24.4%). On this basis, HM-X was selected as the benchmark catalyst for further investigation. LC-MS analysis indicated the formation of isomeric and oligomeric species.

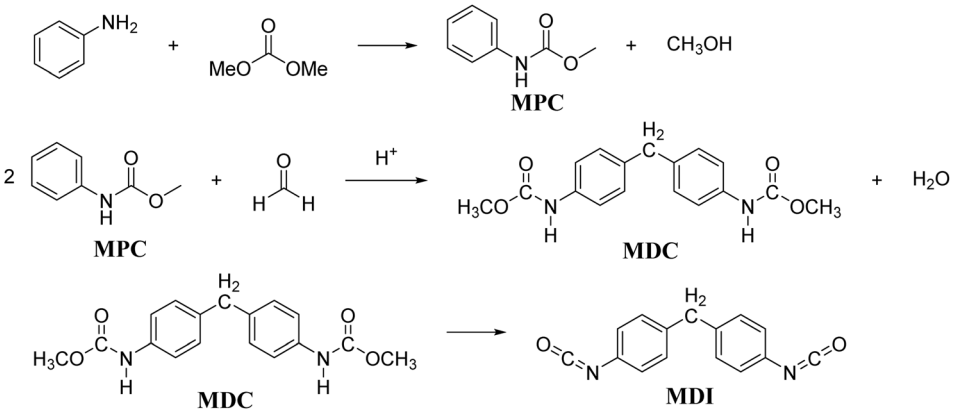

Scheme 1 MDC synthesis from MPC and formaldehyde over solid acid catalysts in DMC under liquid-phase conditions.

Table 1 Single-point screening of acid catalysts for the MPC → MDC condensation[a,b]

Entry	Catalyst label	MDC Yield (%)	MPC Conversion (%)
1	Blank (no catalyst)	N.R.	—
2	K10	41.3	62.8
3	HM-X	76.4	95.2
4	HM-Y	—	14.1
5	H-ZSM-5(Si/Al = 40)	9.1	51.3
6	ZSM-5	9.8	52.3
7	Sn-beta	—	40.9
8	Acidic clay (Huangshan)	20.0	50.4
9	Acidic clay (Anji)	54.5	72.1
10	MCM-22	24.4	39.6
11	HY/9–12	2.6	26.6

[a] Reaction conditions: MPC 10 mmol; formaldehyde, 37% (w/w) aqueous, n(MPC)/n(HCHO) = 4; DMC 20 mL; catalyst 1.0 g, 90 °C, 4 h. [b] N.R.: No reaction.

3.2. Catalysts characterization

To better understand the catalytic performance and to provide a reference, the commercial acid-treated clay HM-X and the as-received montmorillonite K10 were subjected to physicochemical characterization by XRD, FT-IR, N_2 adsorption–desorption, NH_3-TPD, and pyridine-IR spectroscopy. The powder XRD patterns of K10 and HM-X are shown in Fig. 1. K10 displayed the characteristic reflections of crystalline montmorillonite, indicating that the layered aluminosilicate structure was preserved. HM-X retained the main features of the montmorillonite pattern, but its diffraction peaks were broader and less intense than those of K10, suggesting a lower apparent crystallinity and increased structural disorder after acid treatment.

The FT-IR spectra of K10 and HM-X are shown in Fig. 2. Both materials display a broad band in the 3600–3200 cm^{-1} region and a band at 1630 cm^{-1}, which are attributed to O–H stretching and H–O–H bending vibrations of hydroxyl groups and adsorbed water, respectively. Compared with K10, HM-X exhibits a more intense band at 3625 cm^{-1}, indicating a higher concentration of surface hydroxyl groups after acid treatment. In the fingerprint region, both samples show the characteristic Si–O stretching vibration at approximately 1035 cm^{-1}. Compared with K10, HM-X exhibits additional or more pronounced bands at 1402, 915, 790, and 572 cm^{-1}. The band at 915 cm^{-1} is commonly assigned to Al–Al–OH or Al–Mg–OH bending vibrations; 790 cm^{-1} to symmetric Si–O–Si stretching; and 572 cm^{-1} to Si–O–Al bending vibrations. The band at 1402 cm^{-1} is associated with surface hydroxyl or framework environment variations.

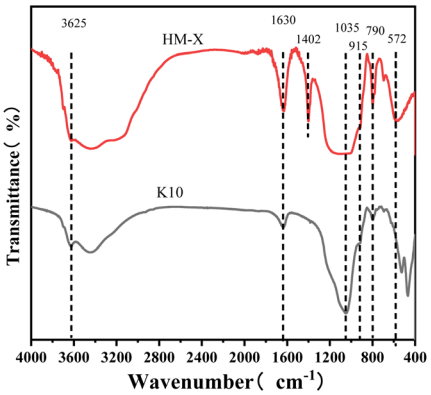

Fig. 2 FTIR spectra of HM-X and K10.

The N_2 adsorption–desorption isotherms of K10 and HM-X are shown in Fig. 3. Both materials exhibit type IV isotherms with a hysteresis loop at intermediate relative pressures, characteristic of mesoporous aluminosilicate clays. BET analysis gave surface areas of 254 $m^2\ g^{-1}$ and 237 $m^2\ g^{-1}$ for K10 and HM-X, respectively, with corresponding total pore volumes of 0.398 and 0.336 $cm^3\ g^{-1}$ and average pore diameters of about 5–6 nm (Table S2). These results indicate that acid treatment preserves the mesoporous texture of the clay and leads only to a slight decrease in surface area and pore volume.

The NH_3-TPD profiles of K10 and HM-X are shown in Fig. 4. Both materials display three desorption regions, which can be assigned to weak (100–200 °C), medium-strength (350–450 °C) and strong (450–600 °C) acid sites. In all three regions the signals of HM-X are markedly more intense than those of K10. Peak deconvolution (Table S3) gives total acid amounts of 9.39 and 32.70 mmol g^{-1} and surface acid densities of 0.037 and 0.138 mmol m^{-2} for K10 and HM-X, respectively. The amounts of weak, medium and strong sites increase from 2.42, 0.79 and 6.18 mmol g^{-1} for K10 to 7.99, 5.52 and 19.19 mmol g^{-1} for HM-

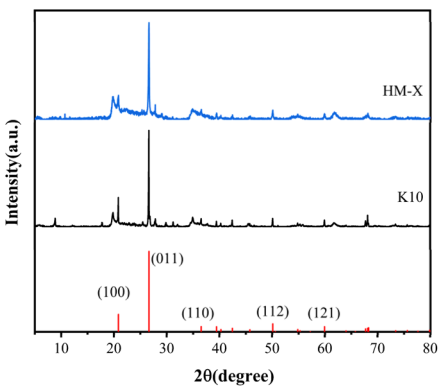

Fig. 1 XRD patterns of HM-X and K10.

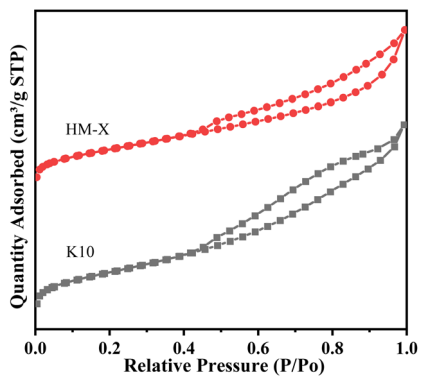

Fig. 3 N_2 adsorption–desorption isotherms of HM-X and K10.

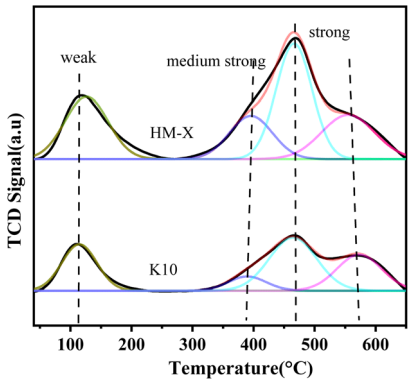

Fig. 4 NH_3-TPD profiles of HM-X and K10.

X. Thus acid treatment greatly enhances the overall acidity, particularly the population of medium and strong acid sites, in line with the higher catalytic activity of HM-X in the MPC condensation.

Pyridine-adsorbed FT-IR spectra of HM-X (Fig. 5 and Table S4) show three characteristic bands at 1445, 1489 and 1540 cm^{-1}. The band at 1445 cm^{-1} is attributed to pyridine coordinated to Lewis acid sites, the band at 1540 cm^{-1} to pyridinium ions on Brønsted acid sites, and the intermediate band at 1489 cm^{-1} is a composite feature that contains contributions from both environments. Quantitative analysis of the 1445 and 1540 cm^{-1} bands gives a B/L ratio of 0.427 at 90 °C, indicating that HM-X is predominantly Lewis acidic under reaction-relevant conditions but retains a significant Brønsted component. When the temperature is increased to 150 °C, the Lewis-related band at 1445 cm^{-1} decreases more strongly than the Brønsted band at 1540 cm^{-1} and the B/L ratio rises to 0.825, which reflects the higher thermal stability of pyridine bound to Brønsted sites. Together with the NH_3-TPD data, which reveal a high density of medium and strong acid sites, these results suggest that a Lewis-acid-dominant surface is beneficial for MDC selectivity, whereas the presence of robust Brønsted sites facilitates the proton-catalysed condensation steps and contributes to the high overall activity, highlighting the importance of both total acidity and an appropriate B/L balance for optimal MPC condensation.

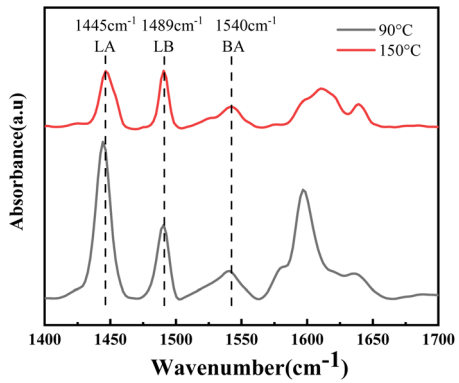

Fig. 5 Pyridine-adsorbed FTIR spectrum of HM-X recorded at 90 °C and 150 °C.

3.3. Catalytic performance of HM-X

Under identical baseline conditions (MPC 10 mmol; DMC 20 mL), the catalytic performance of HM-X was optimized by varying individual parameters (Fig. 6).

Reaction temperature (Fig. 6a). Raising the temperature from 75 to 95 °C increased MPC conversion monotonically, while the MDC yield passed through a broad maximum at 90 °C and declined slightly at 95 °C. A reaction temperature of 90 °C was therefore selected.

Initial molar ratio n(MPC)/n(HCHO) (Fig. 6b). Increasing the ratio from 4 to 10 enhanced both conversion and MDC yield, with only marginal gains beyond 10. The improvement is attributed to suppression of formaldehyde-driven side reactions (*e.g.*, oligomerization, acetalization) at lower aqueous-formaldehyde levels. Although the highest yield occurred at 10, a value of 7 was adopted to limit excess MPC while maintaining near-optimal performance.

Catalyst dosage (Fig. 6c). Conversion rose modestly with increasing catalyst mass, whereas MDC yield showed a shallow maximum at ~1.5 g and then decreased slightly at higher loadings, suggesting that excessive acidity promotes non-productive pathways or re-adsorption of intermediates.

Reaction time (Fig. 6d). Extending the reaction from 3.0 to 5.0 h increased conversion. The MDC yield rose sharply between 3.0 and 4.0 h, then plateaued and declined slightly by 5.0 h, consistent with competing reactions at extended residence times.

On this basis, the optimized parameters for HM-X are n(MPC)/n(HCHO) = 7, 90 °C, 4.0 h, and a catalyst dosage of 1.5 g, which deliver a high and reproducible MDC yield with near-quantitative MPC conversion.

Reaction conditions: (a) MPC 10 mmol; formaldehyde, 37% (w/w) aqueous; n(MPC)/n(HCHO) = 4; DMC 20 mL; catalyst 1.0 g; t = 4 h. (b) MPC 10 mmol; formaldehyde, 37% (w/w)

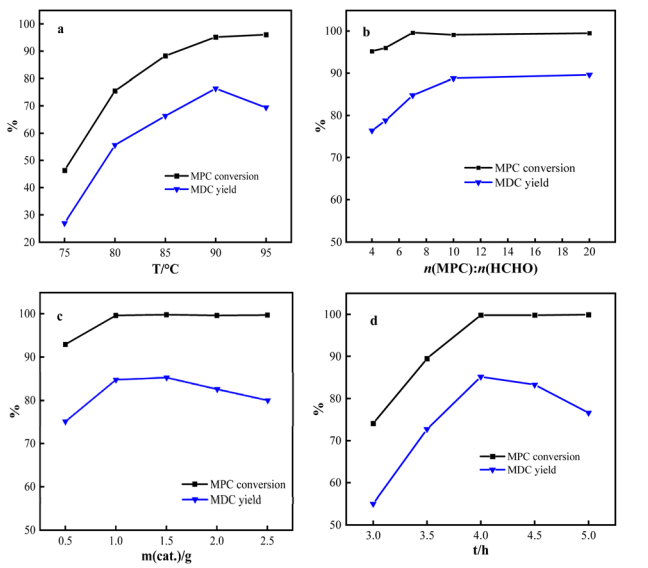

Fig. 6 Effect of reaction parameters on the catalytic performance of HM-X: (a) reaction temperature; (b) initial molar ratio n(MPC)/n(HCHO); (c) catalyst dosage; (d) reaction time.

aqueous; catalyst 1.0 g; DMC 20 mL; $T = 90°$; $t = 4$ h. (c) MPC 10 mmol; formaldehyde, 37% (w/w) aqueous; n(MPC)/n(HCHO) = 7; DMC 20 mL; $T = 90°$; $t = 4$ h. (d) MPC 10 mmol; formaldehyde, 37% (w/w) aqueous; n(MPC)/n(HCHO) = 7; DMC 20 mL; catalyst 1.5 g; $T = 90$ °C.

The fresh HM-X catalyst afforded an MDC yield of 85.2% at 99.8% MPC conversion with 85.4% selectivity. After five reuse cycles, the values remained essentially unchanged (99.5% conversion, 84.8% yield) (Fig. S11b). Both acidity and textural properties remained essentially constant within experimental uncertainty, with total acidity changing only from 32.702 to 32.512 mmol g^{-1}, acid-site density from 0.138 to 0.137 mmol m^{-2}, S_{BET} from 236.91 to 235.71 $m^2\ g^{-1}$, V_p from 0.336 to 0.328 $cm^3\ g^{-1}$, and average pore diameter from 5.675 to 5.672 nm.

In comparison, a series of TPA-loaded K10 catalysts were prepared and evaluated against the commercial acid clay HM-X (Table S1). The optimized TPA/K10 catalyst achieved an MDC yield of 80.5% with 90.2% MPC conversion under the optimized reaction conditions (Fig. S6–S10), demonstrating slightly lower yield and conversion to HM-X.

HM-X consistently achieved higher MPC conversion than TPA/K10 under comparable conditions. However, the corresponding MDC yield was more sensitive to variations in reaction temperature, catalyst dosage, and residence time. This trend can be rationalized by the higher density and strength of acid sites on HM-X, which enhance overall catalytic activity but may also facilitate competing secondary reactions under certain conditions. In contrast, the TPA/K10 catalyst, characterized by lower acidity and reduced surface acid density (Tables S2–S4), exhibited comparatively stable MDC yields across the tested conditions, albeit with lower overall conversion. These results indicate that catalytic activity correlates with the number and accessibility of acid sites (HM-X > TPA/K10), whereas sustained selectivity and optimal yield depend more critically on a balanced distribution of acid strength and an appropriate Brønsted/Lewis acidity ratio.

3.4. Reaction mechanism and role of acid-site types

Under liquid-phase conditions, condensation of MPC with formaldehyde proceeds *via* an acid-catalyzed electrophilic pathway (Scheme 2a). In the first step, formaldehyde is activated on Brønsted acid sites to form a protonated (oxonium) species, which increases the electrophilicity of the methylene carbon and lowers the barrier for nucleophilic attack.[12] The aromatic ring of MPC then attacks the activated carbonyl to generate a methylene-bridged carbamate intermediate, which subsequently evolves into MDC through deprotonation and water elimination. In this sequence, Brønsted acidity directly promotes oxonium formation, so it is crucial for overcoming the kinetic bottleneck associated with carbonyl activation.

Lewis acid sites complement this role by polarizing the carbonyl group and stabilizing cationic (arenium or benzylic) intermediates, thereby influencing the relative rates of competing elementary steps. This contribution can help to suppress unproductive channels such as consecutive condensations, acetalization or transesterification involving DMC, and

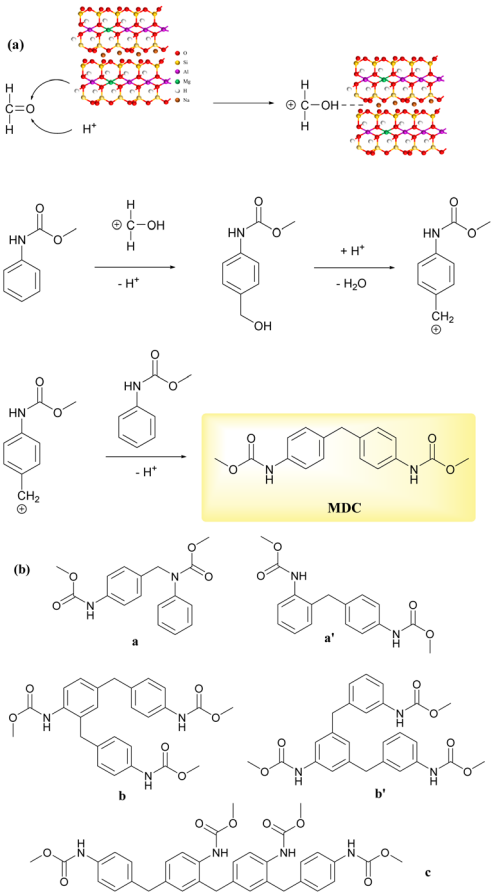

Scheme 2 (a) Proposed reaction mechanism for MDC synthesis from MPC and formaldehyde; (b) by-products detected in the reaction system.

oligomerization of carbamate species.[33] The combined NH_3-TPD and pyridine-IR data show that HM-X possesses a high density of medium and strong acid sites and is Lewis-acid-dominant at 90 °C, while still exhibiting a significant Brønsted fraction. Such an acidity pattern is consistent with efficient formaldehyde activation by Brønsted sites, together with Lewis sites that tune intermediate stability and favor MDC formation. When the overall acid strength or the density of accessible sites is too high, however, consecutive transformations are promoted, leading to reduced MDC selectivity at nearly complete MPC conversion.[11,36] This behavior is in line with previous reports on supported heteropoly acids and acidic clays, which highlight that both sufficient Brønsted strength and a moderated Lewis contribution, together with an appropriate B/L ratio on montmorillonite-based supports, are required to achieve high activity and selectivity under mild conditions.[16,37]

The main by-products observed in the MPC–HCHO condensation in DMC are summarized in Fig. S13 and Scheme 2b. Species a and a′ originate from transesterification or acetalization involving DMC or trace methanol, b and b′ arise from secondary condensation reactions between carbamate intermediates, and c corresponds to higher oligomeric urethane-type

products. These side-products are characteristic of strongly acidic environments and account for the loss of MDC selectivity when acidity is excessive, further underscoring the need to control both total acidity and the Brønsted/Lewis balance.

3.5. Scale-up evaluation over HM-X

Scale-up experiments were carried out to assess the performance of HM-X under process-relevant conditions. The reaction was conducted in a 2 L four-neck flask, in which MPC (80.0 g) and HM-X (60.0 g) were charged together with DMC (1200 mL). The mixture was heated under mechanical stirring (200 rpm). After reaching 70 °C, 37 wt% aqueous formaldehyde (6.14 g) was added dropwise over 30 min, followed by further heating to 90 °C and refluxing for 6 h. At the optimized catalyst dosage of 60.0 g, HM-X afforded an MDC yield of 88.1% while maintaining high selectivity.

4. Conclusion

A commercial acidity clay HM-X was used for the phosgene-free condensation of MPC with formaldehyde to produce MDC in DMC. Characterization techniques, including XRD, N_2 adsorption–desorption, NH_3-TPD, and pyridine-IR spectroscopy, were performed to analyze the structural and acid-site properties of HM-X. Catalytic testing demonstrated that acidity controls both the reaction rate and pathway selectivity: excessive acidity or high site density promotes consecutive condensation, acetalization, and oligomerization, which reduces MDC selectivity. Under the studied conditions, HM-X achieved high activity and MDC yield. In scale-up experiments, HM-X delivered an MDC yield of 88.1%. Mechanistic analysis showed that Brønsted sites mediate formaldehyde activation (*via* oxonium formation), while a balanced Lewis component stabilizes carbocation intermediates and limits side reactions.

Conflicts of interest

There are no conflicts to declare.

Data availability

All relevant data supporting the findings of this study are included in the article and its supplementary information (SI). For further information or additional experimental details, please contact the corresponding author. Supplementary information: experimental details and additional data. See DOI: https://doi.org/10.1039/d5ra09318j.

Acknowledgements

This work was supported by Advanced Catalysis and Green Manufacturing Collaborative Innovation Center of Changzhou University. This work was supported by Changzhou Municipal Science and Technology Bureau (CJ20240054).

References

1 J. Ae Lim, Y.-W. You, S. Kwon Kang, J. Rho, S. Yeo, S. Han, M. Im, U. Young Kim, M.-C. Kim, T.-S. Chang, J. Hoon Park, J. An and J. Hee Lee, *Chem. Eng. J.*, 2024, **494**, 153012.
2 J. Niesiobędzka and J. Datta, *Green Chem.*, 2023, **25**, 2482–2504.
3 F. Campana, G. Brufani, F. Mauriello, R. Luque and L. Vaccaro, *Green Synth. Catal.*, 2025, **6**, 217–238.
4 H. van den Berg, L. van der Ham, H. Gutierrez, S. Odu, T. Roelofs and J. de Weerdt, *Chem. Eng. J.*, 2012, **207–208**, 254–257.
5 P. Tundo and M. Selva, *Acc. Chem. Res.*, 2002, **35**, 706–716.
6 D. Shi, S. Heyte, M. Capron and S. Paul, *Green Chem.*, 2022, **24**, 1067–1089.
7 D. Stoian, T. Sugiyama, A. Bansode, F. Medina, W. van Beek, J.-y. Hasegawa, A. Nakayama and A. Urakawa, *Chem. Sci.*, 2023, **14**, 13908–13914.
8 H. Ohno, M. Ikhlayel, M. Tamura, K. Nakao, K. Suzuki, K. Morita, Y. Kato, K. Tomishige and Y. Fukushima, *Green Chem.*, 2021, **23**, 457–469.
9 W. Xu, Z. Xu, W. Yao, L. Hu, K. Ding, G. Wu, G. Xiao and L. Gao, *Appl. Catal. A-Gen.*, 2023, **662**, 119262.
10 C. W. Lee, S. M. Lee, T. K. Park, K. H. Park and J. S. Lee, *Appl. Catal.*, 1990, **66**, 11–23.
11 F. Li, R. Min, J. Li, L. Gao, W. Xue, Y. Wang and X. Zhao, *Ind. Eng. Chem. Res.*, 2014, **53**, 5406–5412.
12 A. V. Tran, H. J. Lee, J. H. Baik, J. Baek and Y. J. Kim, *Catal. Lett.*, 2021, **152**, 2206–2214.
13 F. Li, H. Xu, W. Xue, Y. Wang and X. Zhao, *Chem. Eng. Sci.*, 2015, **135**, 217–222.
14 E. S. Vasiliadou, N. S. Gould and R. F. Lobo, *ChemCatChem*, 2017, **9**, 4417–4425.
15 W. Wu, C. Deng, Q. Lei and H. Chen, *New J. Chem.*, 2023, **47**, 13993–14001.
16 L. Chen, B. Nohair and S. Kaliaguine, *Appl. Catal., A*, 2016, **509**, 143–152.
17 T. Li, H. Li, G. Qin, H. Liu and Y. Pei, *Front. Chem. China*, 2010, **5**, 99–103.
18 L. I. U. Limin, L. I. Fang, W. Yanji and Z. Xinqiang, *Chin. J. Catal.*, 2007, **28**, 667–669.
19 G. Yanlou, H. U. Liyan, Z. Xinqiang, A. N. Hualiang and W. Yanji, *Chin. J. Chem. Eng.*, 2009, **17**, 756–760.
20 H. Shen, Y. Zhou, G. Wen, L. Xu, Q. Ding, Y. Guan, Z. Yang, Y. Sun, X. Gao, J. Zhang, X. Fan and Y. Jiao, *Biomass Bioenergy*, 2022, **165**, 106552.
21 Y. Patiño, L. Faba, E. Díaz and S. Ordóñez, *J. Environ. Manage.*, 2024, **365**, 121643.
22 C. R. Reddy, Y. S. Bhat, G. Nagendrappa and B. S. J. Prakash, *Catal. Today*, 2009, **141**, 157–160.
23 P. V. Kumar and G. Madhumitha, *RSC Adv.*, 2024, **14**, 4810–4834.
24 B. S. Kumar, A. Dhakshinamoorthy and K. Pitchumani, *Catal. Sci. Technol.*, 2014, **4**, 2378–2396.
25 N. Horri, E. S. Sanz-Pérez, A. Arencibia, R. Sanz, N. Frini-Srasra and E. Srasra, *Adsorption*, 2020, **26**, 793–811.

26 M. Śliwa, K. Samson, M. Ruggiero-Mikołajczyk, A. Żelazny and R. Grabowski, *Catal. Lett.*, 2014, **144**, 1884–1893.
27 E. Vyskočilová, E. Vrbková, J. Trejbal, M. Vaňková and L. Červený, *Catal. Lett.*, 2022, **152**, 1417–1427.
28 M. Baikousi, A. Stamatis, M. Louloudi and M. A. Karakassides, *Appl. Clay Sci.*, 2013, **75**, 126–133.
29 M. N. Timofeeva, *Appl. Catal., A*, 2003, **256**, 19–35.
30 A. D. Newman, A. F. Lee, K. Wilson and N. A. Young, *Catal. Lett.*, 2005, **102**, 45–50.
31 P. M. Rao, A. Wolfson, S. Kababya, S. Vega and M. V. Landau, *J. Catal.*, 2005, **232**, 210–225.
32 I. V. Kozhevnikov, K. R. Kloetstra, A. Sinnema, H. W. Zandbergen and H. v. van Bekkum, *J. Mol. Catal. A Chem.*, 1996, **114**, 287–298.
33 V. Zholobenko, C. Freitas, M. Jendrlin, P. Bazin, A. Travert and F. Thibault-Starzyk, *J. Catal.*, 2020, **385**, 52–60.
34 C. A. Emeis, *J. Catal.*, 1993, **141**, 347–354.
35 L. Rodríguez-González, F. Hermes, M. Bertmer, E. Rodríguez-Castellón, A. Jiménez-López and U. Simon, *Appl. Catal., A*, 2007, **328**, 174–182.
36 E. Hosgor, C. K. Lee, N. Capra, W. Verboom, J. P. Lange and J. Huskens, *Mol. Catal.*, 2024, **556**, 113930.
37 Q. Zhu, J. Zhu, Y. Li, Z. Zhang, B. Wang and J. Ma, *Appl. Catal., A*, 2023, **649**, 118942.